STUDY OF THE FRACTURE BEHAVIOR OF FIBER REINFORCED CONCRETE UNDER DIRECT SHEAR LOADING

Fatemeh Soltanzadeh, Joaquim António Oliveira de Barros and Rafael Francisco Cardoso Santos

Report 12-DEC/E-18

The present report is part of the research Project entitled "DURCOST – Innovation in reinforcing systems for sustainable prefabricated structures of higher durability and enhanced structural performance" supported by FCT and with the reference PTDC/ECM/105700/2008.

Date: May 2012

Pages: 35

Keywords: Fiber reinforced self-compacting concrete, Mode II of fracture, stress intensity factor, image analyzing.

School of Engineering

Department of Civil Engineering

University of Minho

Fundação para a Ciência e Tecnologia

CONTENTS **Page No.**

Summary: The behavior of Fiber Reinforced Concrete (FRC) under Mode II of fracture is rarely reported due to the lack of information on standard testing procedures. Between the few numbers of researches performed to characterize the shear behavior of concrete, no one have dedicated to the effects of fiber orientation at different places of a concrete element subjected to second mode of fracture. In addition the efforts made on mode II loading effects are rather limited in plain concrete in general and in fiber reinforced concrete in particular.
In the present study the double shear specimen (DSS) has been used to characterize the shear behavior of Fiber Reinforced Self Compacting Concrete (FRSCC). Considering the effects of fiber orientation on Mode II of fracture, some beams $150 \times 150 \text{mm}^2$ cross section and 60mm length has been discretized in to 8 or 12 specimens included different shear sections. Using the designed specimen, fracture energy and toughness, stress intensity factor and shear stress-slip relationship is calculated along the beams. The results show that none of the specimens are subjected to pure Mode II due to the considerable ratio of the stress intensity factors in first mode of fracture to that of the second mode " $\frac{K_I}{K_{II}}$."
Unlike the crack propagation in mode I of fracture, the shear crack propagation is accompanied by compression failure after the maximum load. The fiber bridging not only restrains the crack opening but also leads to higher interlocking. Furthermore, the dowel action of the fibers, leads to a lower slip and higher shear transfer. The suitable fracture energy and consequently high toughness is detected not only at the middle of the beam but even in the case of the specimen located at the farther distances from the center of the beam. It is indicated that using the proper Self Compacting Concrete (SCC) mix can be helpful to have the uniform shear behavior along the beam. Additionally increasing the shear plane appears to have an increasing trend in ductility, rate of fracture and toughness of the specimens.
Furthermore, the orientation and distribution of fibers in concrete is investigated by the help of image analyzing. It is observed that fibers dispersed homogeneously in all concrete series. Although the density of the fibers detected on the shear plane of all the specimens is almost the same, the ductility of the specimens is different. It shows that the ductility of the specimens can be affected by the area of the shear plane.

1 INTRODUCTION

Classical fracture mechanics defines three basic modes of fracture named as Mode I or opening mode, Mode II or sliding mode and Mode III or tearing mode. Since the basic concepts of fracture mechanics has been developed, the crack opening mode of fracture is studied analytically and experimentally. The mixed Mode I/II problems have also received some attention; while a few investigations have been conducted in connection with Mode II of fracture [1].
According to Ayatollahi et al. [2], pure shear loading is defined as a loading condition in which a specimen is subjected to equal and opposite parallel forces with negligible bending. Some researchers [3] do not accept the existence of mode II failure in concrete. It is due to the easy failure of concrete in mode I. In this condition the crack tends to follow the maximum principal stress and develops perpendicularly to that stress. Some others [4] expressed that mode II failure exists in cases where the shear stress zone is

narrow enough. The criterion for crack extension is then the maximum energy release rate rather than the maximum principal stress. Thus many researchers have been directed to modeling the crack propagation and fracture in concrete subjected to the mixed mode loading [5]. Due to such a loading the crack and its "tip" are subjected to the combine stresses. The deformation at the crack tip may have both Mode I and Mode II component. This influence on the process of cracking may be of great importance in the concrete structures [5].

Recently the use of fibers in structural application has been pronounced as shear reinforcement to avoid brittle failures. The main intention is that the addition of discontinuous fibers converts brittle concrete matrix in to more homogenous and isotropic matrix [6]. Addition of steel fibers can improve the post cracking energy absorption capacity of concrete which is usually designated by toughness [7]. Steel fibers have the positive effect on concrete ductility, cracking control and tensile strength as well as reduction of shear deformations at all stages of loading [6]. These advantages vary according to the type and volume of fiber added to the matrix. Unlike the tensile strength of concrete the concrete ability to control the cracks and ductility improves even by addition of very low fiber volumes (under 0.5%) [8]. Increased ductility is associated mostly with successive pull-out of the fiber, which uses large amounts of energy. The influence of fibers on shear strength can be associated with two factors: direct action on inclined cracks (in a similar way to stirrups) and the indirect contribution on the transfer mechanism of transverse forces, which increase concrete strength contribution (dowel effect of the longitudinal reinforcement and crack friction) due to improved control of cracking [9]. However, improving the concrete characteristic using fiber is sensitive to fiber orientation. Thus, the development of non-uniform crack opening has been reported since the fibers segregation occurs easily due to the vibration [7]. To detect the fractural behavior of steel fiber reinforced concrete, the fiber orientation should be characterized through the complete distribution and regular orientation angles occurring at the crack-bridging zone [10]. Using Self Compacting Concrete (SCC) can provide such a suitable condition, although the wall effect is always there.

To characterize the fracture mechanism of concrete, the proper test specimen and set up should be used. Since the effort of this study is to characterize the fiber reinforced concrete under direct shear loading, it is tried to design the shear specimen.

In general, the tests performed to study the shear behavior of Fiber Reinforced Concrete (FRC) can be categorized in to two groups: direct shear tests and tests on beam and corbels [10]. The direct shear test are required to study mode II fracture parameters while the stress on beam and corbels are necessary to understand the behavior of FRC structures [6].

In the recent years, many researchers [5, 11-31] have carried out modes I, II and the mixed modes fracture tests for different material on new specimen geometry. Between the few numbers of researches performed to characterize the shear behavior of concrete, no one have dedicated to the effects of fiber orientation at different places of a concrete element subjected to second mode of fracture. In addition the efforts made on mode II or mix mode loading effects are rather limited in plain concrete in general and in fiber reinforced concrete in particular.

The purpose of the present work is to investigate the fracture behavior and toughness of FRSCC experimentally. The special attention is paid to include the effects of fiber orientation and collaboration on the concrete fracture behavior subjected to the shear stress. Due to the same objective of the present study the special specimen is designed and made by discretizing a single beam specimen to the smaller pieces. In the present study, the double shear test technique for characterizing the shear behavior of Fiber Reinforced Self-Compacting Concrete (FRSCC) is used. Furthermore, the fracture behavior of the specimen is justified using the image analyzing.

2 TEST SPECIMEN

The simple schematic of Double Shear Specimen (DSS) is shown in Fig.1. In this test configuration, a square specimen of edge length 150mm is loaded vertically. It contains four notches of length 25mm which are placed at the top and bottom edges of the specimen. The shear planes are placed along the ligaments and connected the notches together. To study the effect of fibers on the fracture behavior of FRSCC, two different thicknesses (b = 50 and 75mm) are chosen for the specimens. The dimensions of the shear planes are respectively$20 \times 100,\ 45 \times 100$ and $55 \times 100 mm^2$.

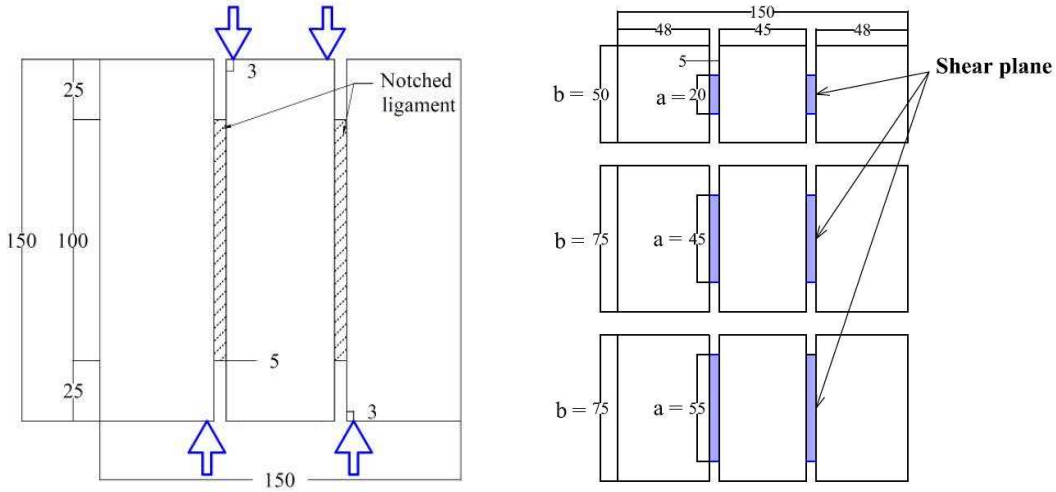

Fig. 1 Geometry and configuration of DSS: (left) front view and (right) top view

2.1 Analytical Studies

Before performing the test, the geometry of the specimen with $20 \times 100 mm^2$ shear plane is analyzed using the finite element program, Femix. The simulated specimen includes 3 different kinds of elements, named as interface element, notched and un-notched elements as shown in Fig. 2 (left).

The interface element can be defined as the element placed along the ligaments of the specimen, at the distance between the tips of the vertical notches. The notched elements which look like the strips with 5mm width are placed beside the interface elements. The rest of the model includes the un-notched elements.

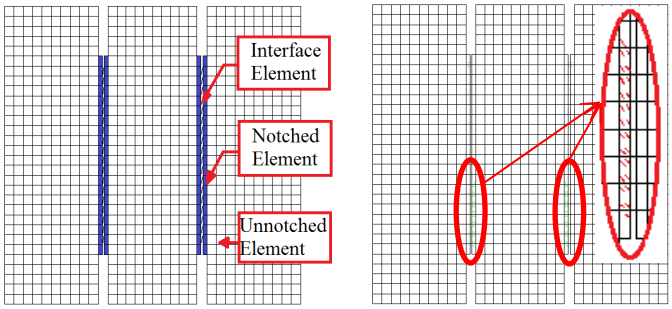

Fig.2 (left) Simulation of the specimen using finite element method (right) Specimen crack pattern

Due to the loading condition, two respective points along each two notch tips slide relative to the ligament. Fig. 2 (right) shows the crack pattern due to the same sliding. Fig. 3 shows the slip occurred at the location of the interface element only, where the cracks appear at the failure moment. The stress distribution is symmetrically due to the application of the symmetric load (Fig. 4). However the fracture of the specimen is not due to the pure shear. The schematic diagram of the beam (Fig.3 (c)) shows the presents of the moment during the fracture of the specimen.

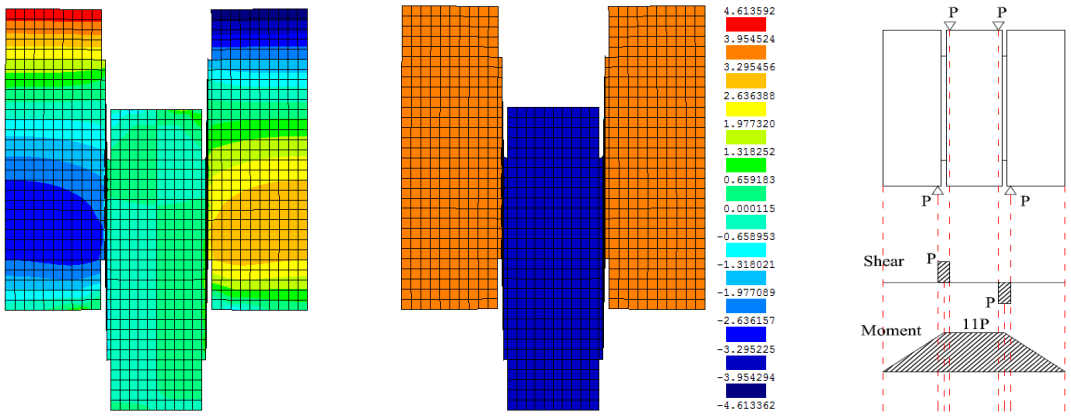

(a) **(b)** **(c)**

Fig. 3 Nonlinear analysis: (a) Displacement of specimen and the critical zone under tension in D2 direction and (b) in D3 direction (c) Schematic of loading diagram

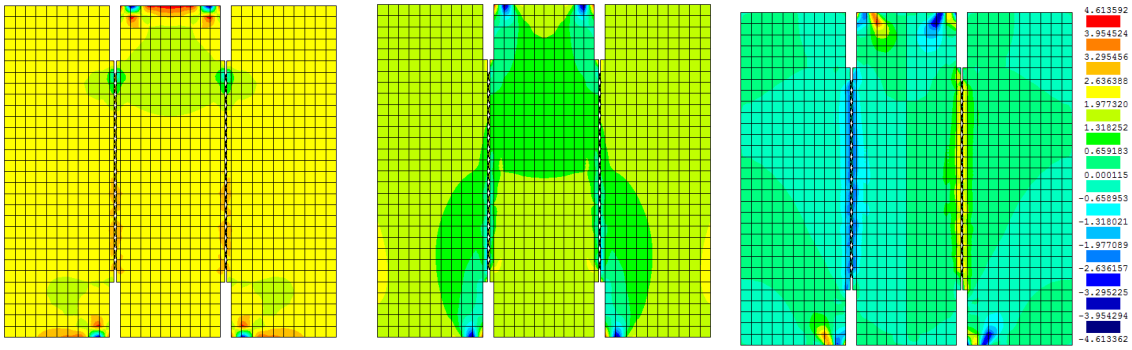

Fig.4 Nonlinear analysis: Principal stresses (from left to right respectively σ_1, σ_2 τ_{12}) at the moment of failure

2.2 Material

In the present study the FRSCC with compressive strength of 65MPa is developed. Portland cement type I 42.5R is used for preparing the mix. Improving the property of the paste, fly ash and lime stone filler is added to the mix. Glenium SKY 617 Super plasticizer which is based on second-generation poly carboxylate ether (PCE) polymers is used to provide the suitable flowability. The crushed granite coarse aggregate, river sand, and fine sand, respectively with 12.5mm 4.75mm and 2.35mm maximum size are included of the aggregate skeleton of the concrete. The concrete is reinforced using the hooked end steel fibers RADMIX RC6535, with 33mm length and aspect ratio of 65. A total of 90 kg/m^3 of fibers were added into the concrete mix. The mix proportions used for preparing of the four RILEM beams $150 \times 150\text{mm}^2$ cross section and 600mm length as per RILEM TC 162-TDF [32], is presented in Table-1. 24 hours after casting, the beams are demolded and cured in the water up to the age of 28 days.

Table-1 FRSCC compositions

Material	Quantity *per m^3*	
Cement	465	Kg
Flay Ash	139	Kg
Lime Stone Filler	139	Kg
Water	208.9	L
Super Plasticizer	15.8	L
Fine Sand	98	Kg
River Sand	693	Kg
Coerce aggregate	500	Kg
Steel Fiber	90	Kg

2.3 Specimen Preparation

Preparing 36 specimens, one beam is discretized in to 12 pieces 50mm thick, including $20 \times 100mm^2$ shear section. Two casted beams have been discretized in to 8 pieces of specimens 75mm thick with $45 \times 100\ mm^2$ shear plane. Next 8 pieces of the same specimens 75mm thick, including $55 \times 100mm^2$ shear plane are made using the last beam.

The pieces located in the same section of the beams are known as one group as shown in Fig.5 (a). Depending on the thickness of the specimens, the beams have been divided in to two or three rows. Due to the symmetric discretization of the beam, at least each two specimen were located exactly at the similar place. Table-2 shows all the details of the specimens.

Since the orientation of the fibers is important, the discretization was such that the orientation of fibers is perpendicular to the shear plane of the specimens. To avoid cracks due to the tensile stresses concentrated at the sides of the specimens (see Fig. 4(a)), the specimens are reinforced using the FRP strips (Fig. 5 (b)).

Fig.5 (a) Location of each specimen along the beam (b) Reinforcing the specimen using FRP strips

Table-2 The details of discretization of the beams

Series No	Location and name of each specimen (Top view)	Thickness of the specimen *Per mm*	Cross section of the shear plan *Per mm²*
B-1	**DSS-1-1** **DSS-2-1** **DSS-3-1** **DSS-4-1** **DSS-1-2** **DSS-2-2** **DSS-3-2** **DSS-4-2** **DSS-1-3** **DSS-2-3** **DSS-3-3** **DSS-4-3**	50	20 × 100
B-2	**DSS-1-1** **DSS-2-1** **DSS-3-1** **DSS-4-1**	75	45 × 100
B-3	**DSS-1-2** **DSS-2-2** **DSS-3-2** **DSS-4-2**	75	45 × 100
B-4		75	55 × 100

3 TEST SETUP AND PROCEDURE

The setup of the shear test is shown in Fig. 6 (left). Two vertical point loads are applied on the middle part of the specimen, pushing this part down. The supports are placed under two outer parts of the specimen near to the notches. This loading condition produces a concentrated shear stress zone along two ligaments of the specimen. To make the moment created due to the eccentricity of the loads negligible; it is attempted to place the supports relatively close to the ligaments. Additionally the special frames have been used to confine the specimen at the points where the stress concentrated due to applying the point loads (see Fig. 4). The top and bottom surface of the specimens are covered using the high strength HILTI HIT-RE 500 epoxy adhesive. The frames and the layer of epoxy, protect the concrete not to shear off locally before the overall shear fracture could be produced.

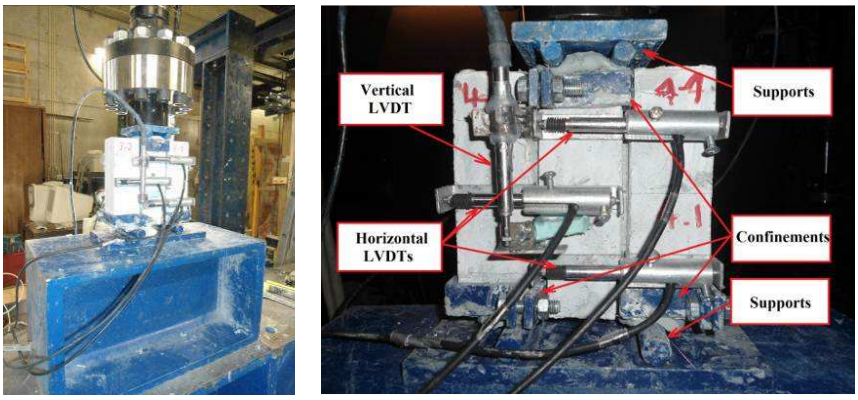

Fig.6 (left) Test setup (right) Location of LVDTs, supports and confinements

The test was conducted under displacement control using the electromechanical testing machine of 100KN capacity. During the tests one LVDT has been recorded the vertical displacement while three others were mentioned the crack openings on each side of the specimen (Fig.6 (right)). This setup has been prepared the possibility of occurrence the shear crack along the ligaments.

4 IMAGE ANALYSIS

The number and orientation of fibers in the cracking area as well as dispersion characteristics of fibers as homogeneous or heterogeneous, generally govern the fracture properties of fiber reinforced concrete. Thus addition to the experimental work has been done in the case of shear behavior of SCC; the fiber structure analysis is performed for DSSs, using an image analysis procedure. This analysis is helpful for having the better justification in the case of the shear behavior of FRSCC specimens.

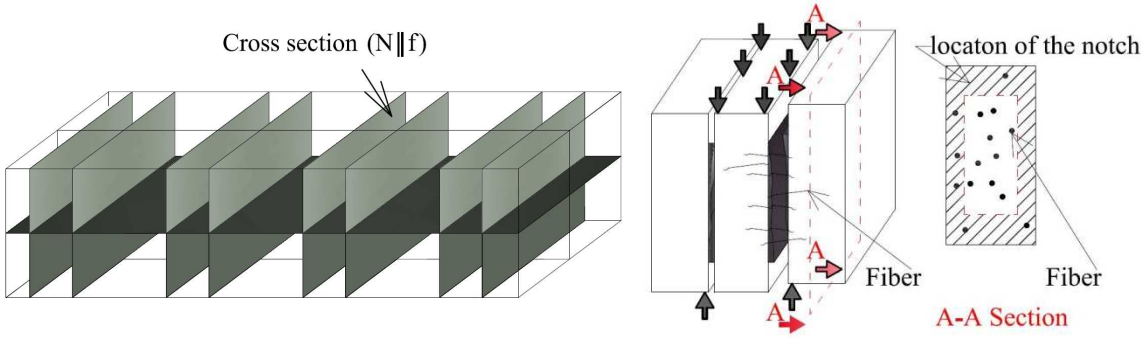

Fig.7 (left) location of the likely cross sections along the beam and (right) Sawn sections of DSS

The fiber counting at the fractured surfaces of the specimens is helpful to capture the density and orientation of the fibers placed along the beams located at the cross sections where the shear cracks have occurred. The localization of the cross sections analyzed in the fiber structure assessment is depicted In Fig.7 (left).

After cutting the cross section of the specimens parallel to the ligament along which the crack is occurred, the fracture surfaces are marked and gently smoothed (Fig.7 (right)). To enhance the visibility of steel fibers, the surfaces are then polished and cleaned using acetone before image capturing Fig.8 (a). Images are collected by high-resolution

camera and processed by image analysis programs. After transforming the photos into a grey scale which is called as pre-processing [36] (Fig.8 (b)), the bright objects are first selected and the images are made binary (Fig.8 (c)). The aggregates which are selected by the program as shining objects are extracted manually from the image. Fig.8 (d) is the final object which is obtained after passing the explained procedure.
In the Post-Processing stage, both the size and coordinates of each fiber particle is determined by the help of the image analysis programs "ImageJ, MicroImage". Moreover the parameters that characterize the fibers such as, global coordinates, minimum and maximum radius and area are analytically computed.

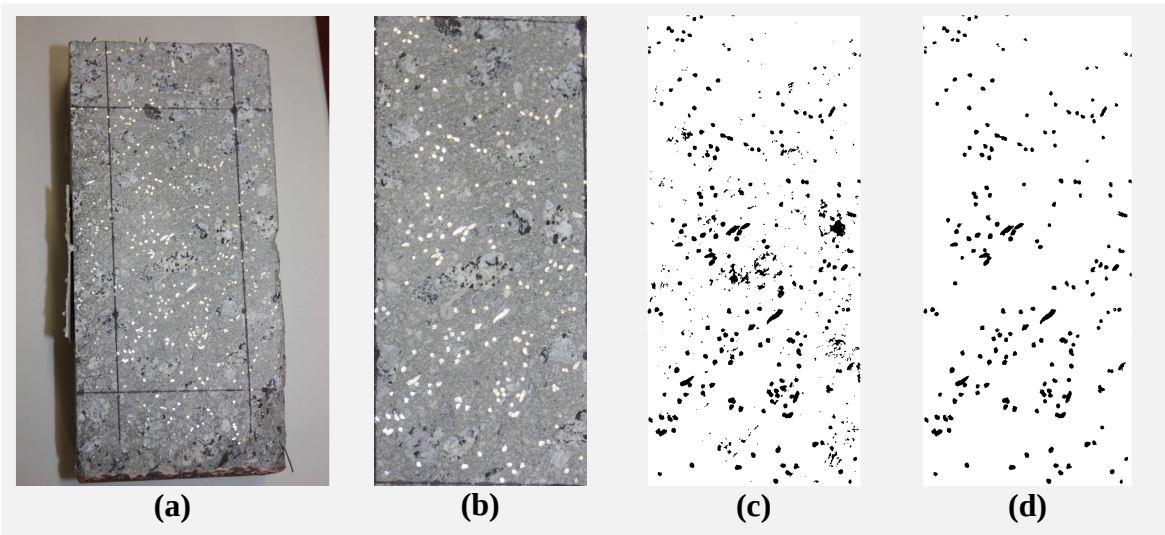

Fig.8 (a) Image of the DSS section including the notches and the shear plane, (b) fibers and some aggregates shown as shining objects on the shear plane (c) binary images, and (d) steel fibers distributed on the shear plane

5 OBSERVATIONS AND RESULTS

5.1 FRSCC Behavior under Direct Shear Loading

Fig. 9 (left) shows the fractured plane has been observed in most of the specimens after failure. It is clear that the cracks do not propagate from the notches in the direction normal to the maximum principal stress; but in the direction in which the shear stress dominates. According to Banzant, Pfeiffer [33], Rao and Rao [22] it demonstrates that the failure of the specimen is in pure mode II along the shear plane considering the preformed notches. However it may not be the sufficient justification for occurrence of such a phenomenon in second mode of fracture.
The failure has occurred slowly due to the fiber pull out during the test. The area of the shear plane, the fiber orientation and dispersion and the maximum energy release rate can be named as the other effective factors on the rate of fracture [22]. For instance the shear fraction has been occurred more rapidly in the case of the specimens in Series B-1which is included the smaller shear sections.

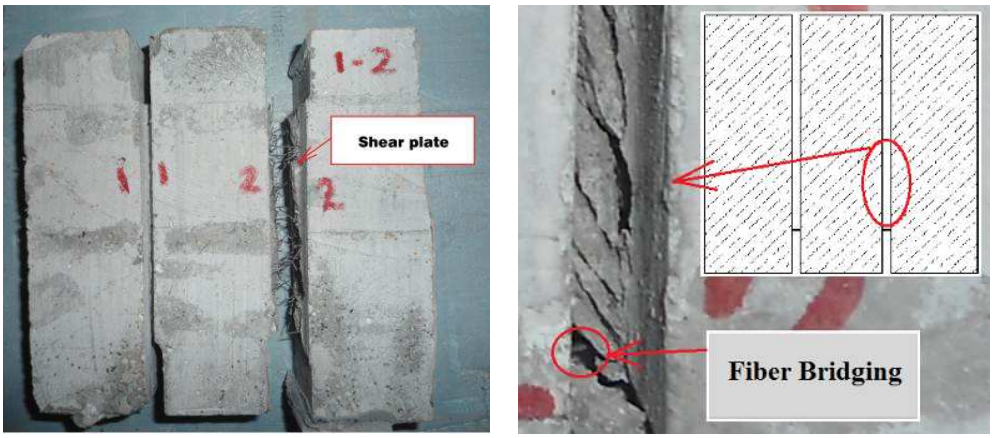

Fig.9 (left) Fractured plane of the specimen (right) Formation of the crack band along the shear plane

The observed failure mode in series B-1, group 4 of the specimens was brittle and in the case of specimen DSS-4-2, almost with no warning before collapse. It might be due to the collaboration of fewer amounts of fibers placed in these sections.
Testing the other specimens with the larger shear section (belonging to series B-2, B-3 and B-4); several small diagonal cracks have been developed as shown in Fig.9 (right). The behavior of the specimens can be expressed in terms of stress versus strain before cracking [34]. Since after cracking localization dominates the behavior; the series of diagonal cracks joined together, forming a crack band along the shear plane. The behavior of the specimen after crack localization can be described as the load versus crack opening or the load versus shear sliding displacement [34] as illustrated in Fig. 10 (c).
Shear sliding causes the activation of the fibers, increasing of the bond stresses along the fibers-concrete interface and gradually fiber deformation and slip. Before the fibers engage and effectively contribute to the strength of the matrix, displacements that would result in excessively wide cracks are needed. Fig. 10 (a) and (b) are shown the performance zones of the fiber and the shear contributions along a single fiber at this moment. The fiber-concrete bond is mostly concentrated at the hooked end and within the snubbing zones. Comparing the components of shear in hooked and snubbing zoon, with that in the straight section of a fiber placed between these two regions, the negligible shear component can be detected for the straight section of fiber [34].
After the crack formation along the ligaments of the specimen, the connection remains across the crack band. It consists of inclined compression struts of concrete between the inclined cracks spanning across the fracture and fibers bridging across the cracks. When this strut is crushed in compression and the fibers are pulled out, the full shear failure occurs.
Unlike the crack propagation in mode I of fracture, the shear crack propagation is accompanied by compression failure along the ligament after the maximum load. The concrete keeps the fibers more tightly and the bond strength between the fiber and the concrete improves. Thus, it is observed that when fibers are collected at one point rather than the other parts of the specimen, the shear crack may change its direction. This phenomenon has been observed in the case of some specimens such as B-1/DSS-4-2 as shown in Fig.11.

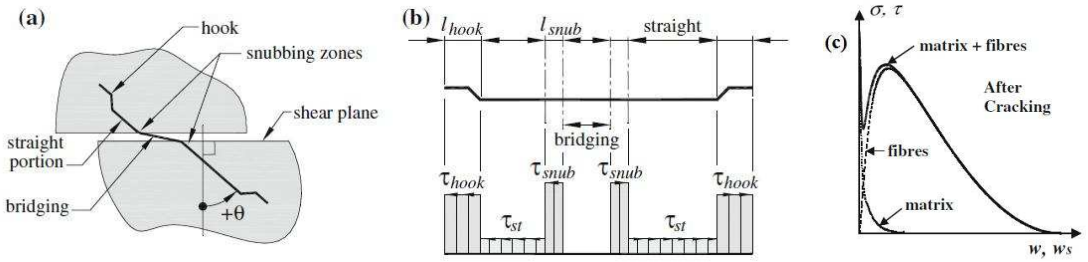

Fig.10 (a) Fiber performance zones (b) shear contributions and (c) crack sliding displacement after cracking for a fiber reinforced cementations material [34]

Increasing the area of the shear section especially in series B-4 of the specimens led to have the different crack behavior. In this series of the specimens, the crack started from the tip of the notches and gradually follows its way out of the ligament. It shows that the stress field near the fracture front, as well as the strain and strain fields near the fracture front does not govern the direction of the fracture propagation. However it can be justified due to the larger number of fibers included in the larger shear section. Thus, the fibers resist the shear cracks along the ligament and shift the crack to the more brittle zone.

Fig. 11 Collection of fibers at one point of shear plane

The results obtained from the shear test performed by some other researchers [5 and 33], has shown the same behavior for the plain concrete and mortar shear prism which is shown in Fig.12 (right). In these tests it is tried to keep the point loads very close to the notches. Founding the crack propagated along the notches, they have proved the existence of Mode II of fracture. Furthermore, they have applied the point loads at the farter distance to the notches and found that the crack direction may change. Thus they have reported that: “for this type of test with the narrow shear force zone, Mode I crack propagating sideway from the notch tip would govern the crack direction. Thus the crack quickly run into the low stress zone of the material and would therefore release little energy. On the other hand the vertically running crack (Mode II) continues to remain in the highly stressed zone of the material and can therefore cause a large release of strain energy. This appears to confirm that the direction of fracture propagation is governed by the criterion of maximum energy release rate [33].”
Comparing the behavior of the crack in series B-4 of the specimens, as shown in Fig.12 (right) with that of studied with the said researchers Fig. 12 (left), one can pointed out

the transition between two different failure modes by varying the thickness of the specimen or the width of the shear plane.
When the specimen is ticker; crack branching is favored and a crack trajectory develops from the crack tip to the opposite point load (like the crack behavior shown in Fig 12 (left) (b) and Fig. 12 (right) (b)). On the other hand, when the thickness is smaller, the ultimate tensile strength is exceeding at the center of the specimen and the crack propagates vertically like the Brazilian splitting test (as shown in Fig. 12 (left) (c) and Fig.12 (right) (a)). However since the ratio of shear plane width to the thickness of the specimens " $\frac{a}{b}$ " is decreased the crack branching seems to be reasonable. Keeping constant the " $\frac{a}{b}$ " ratio for the larger specimen might be helpful to detect the crack along the ligaments only. The fracture behavior of the specimens under the shear load is reviewed in annex A.

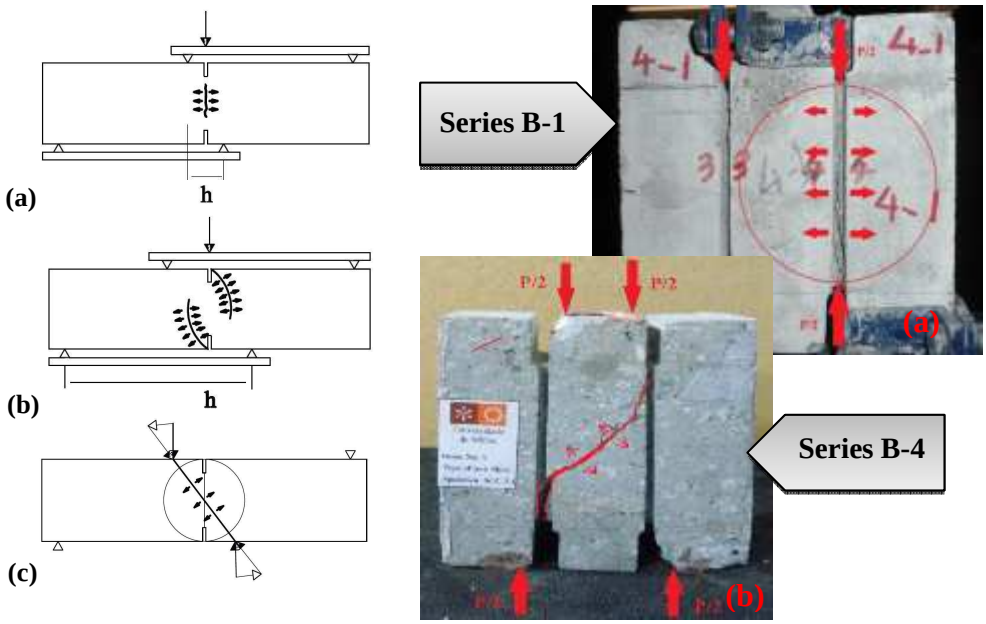

Fig. 12 (left) Shear failure of beam (a) tensile splitting, (b) mixed mode crack propagation and (c) diametrically loaded beam [5 and 33] (right) (a) Crack pattern of series B-1 and (b) B-4 of specimens

The maximum load (P_{max}), the corresponding slip at the pic load (δ_{Pic}) and maximum shear stress (τ_u) obtained by testing each specimen is illustrated as Table-3. The load value is divided in to two in all the calculations. Additionally the value "k" as the correlation constant between the average shear stress and compressive strength (Eq.1) is mentioned in the same table.

$$\tau_u = k\sqrt{f_{cm}} \quad (1)$$

It is clear that by increasing the area of the fracture plane, the maximum load increased respectively. Consequently, the shear stress and the constant "k" have shown the descending trend. It is because of decreasing the ratio of the load to shear plane area in series B-4 as compare to the other series.

Since the beam has been casted by pouring the concrete at the middle of the mold, it was assumed that the average shear stress should decrease by getting distance from the middle of the beam. So that the effect of fibers could be deceased by decreasing the number of fibers located at the ends of the beam. However, the maximum shear stress and consequently the correlation constant “k” did not follow the same role all over the beam. The location of the shear crack which is shown in Table-4 presents the same point. It might be due to the proper flowability, viscosity and homogeneity of the proposed SCC which led to have the uniform distribution and suitable orientation of the fibers along the beam.

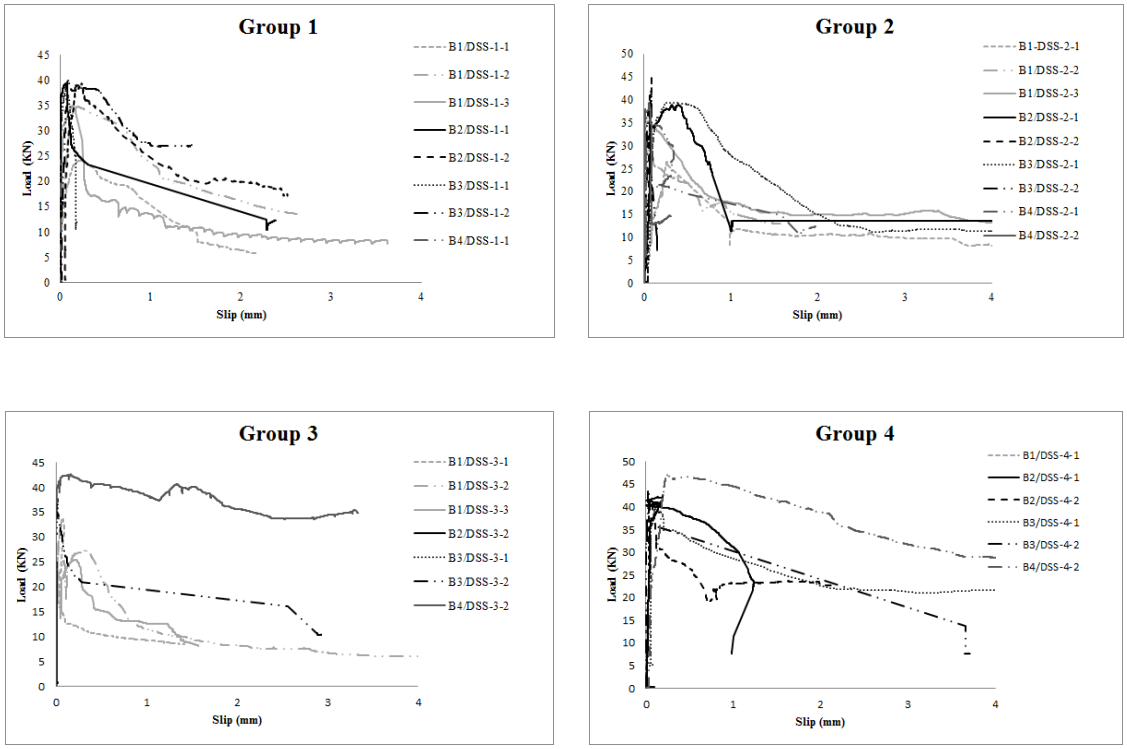

Fig. 13 Load-slip relationship

Fig. 14 shows the typical load-slip relationship under direct shear loading of 4 series of the specimens in different groups. The load-slip response seems to be relatively linear up to occurrence of the first crack. It tends to become nonlinear up to reaching the peak load. After the pic load, the load drops suddenly up to the complete failure. The last stage is faster in the case of first series of the specimens. It might be due to the fact that some steel fiber which bridged the crack along the shear ligament yielded in tension. This behavior has followed by rupture of the fibers upon increase the deformation. According to Vall et al. [35], this yielding and breaking behavior of the fibers resulted primarily due to the improved bond provided by the concrete.

Table-3 Strength and fracture property of FRSCC at the point of pick load

Series No	Specimen No.	P_{max} (KN)	δ_{Pic} (mm)	(τ_u) (MPa)	$K_{Av.}$
B-1	DSS-1-1	24.11	0.2194	12.06	2.0
	DSS-1-2	34.72	0.2044	17.36	
	DSS-1-3	34.89	0.1383	17.45	
	DSS-2-1	17.63	0.2621	10.58	1.8
	DSS-2-2	29.76	0.0788	14.88	
	DSS-2-3	35.55	0.0143	17.78	
	DSS-3-1	22.39	0.0700	16.79	1.8
	DSS-3-2	27.33	0.3160	13.66	
	DSS-3-3	25.34	0.2135	12.67	
	DSS-4-1	25.56	0.0465	12.79	1.7
	DSS-4-2	19.94	0.0000	9.97	
	DSS-4-3	30.27	0.0002	15.14	
B-2	DSS-1-1	39.29	0.0593	9.82	1.2
	DSS-1-2	39.46	0.2293	9.87	
	DSS-2-1	38.90	0.3212	9.72	1.3
	DSS-2-2	45.64	0.0860	?	
	DSS-3-1	41.15	0.0000	10.29	1.3
	DSS-3-2	41.34	0.0646	10.34	
	DSS-4-1	42.48	0.1933	10.62	1.3
	DSS-4-2	41.23	0.0434	10.31	
B-3	DSS-1-1	37.82	0.1241	9.46	1.2
	DSS-1-2	40.13	0.0850	10.03	
	DSS-2-1	39.49	0.3257	9.87	1.3
	DSS-2-2	41.58	0.0916	10.40	
	DSS-3-1	39.57	0.8321	9.89	1.2
	DSS-3-2	37.57	0.0187	9.39	
	DSS-4-1	40.52	0.1287	10.13	1.3
	DSS-4-2	43.32	0.0251	10.83	
B-4	DSS-1-1	36.38	0.0709	7.28	0.9
	DSS-1-2	-	-	-	
	DSS-2-1	38.15	0.0148	7.63	1.0
	DSS-2-2	39.30	0.0539	7.86	
	DSS-3-1	3.62	0.0702	0.723	0.6
	DSS-3-2	42.65	0.1608	8.53	
	DSS-4-1	-	-	-	1.2
	DSS-4-2	9.44	0.2464	9.44	

Table-4 Failure mode and variation of the correlation constant "k" along the beam

Group No. / Series No.	Group 1	Group 2	Group 3	Group 4
B-1	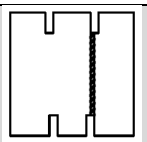 DSS-1-1/K=1.50	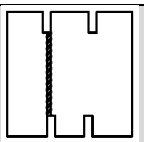 DSS-2-1/K=1.31	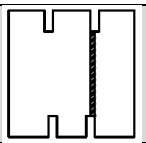 DSS-3-1/K=2.08	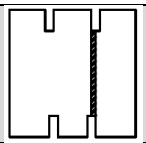 DSS-4-1/K=1.59
	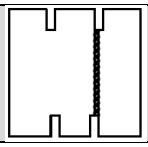 DSS-1-2/K=2.15	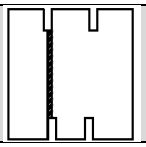 DSS-2-2/K=1.48	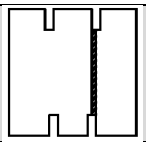 DSS-3-2/K=1.36	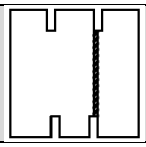 DSS-4-2/K=1.24
	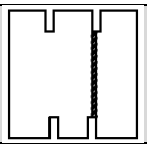 DSS-1-3/K=2.16	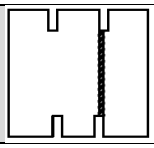 DSS-2-3/K=2.20	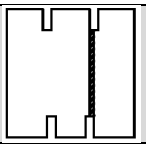 DSS-3-3/K=1.26	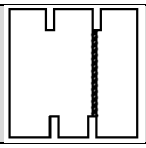 DSS-4-3/K=1.50
B-2	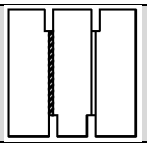 DSS-1-1/K=1.22	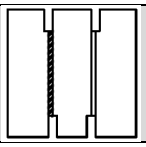 DSS-2-1/K=1.20	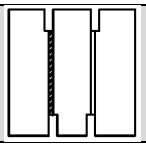 DSS-3-1/K=1.28	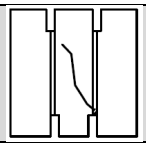 DSS-4-1/K=1.32
	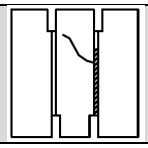 DSS-1-2/K=1.22	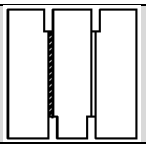 DSS-2-2/K=1.42	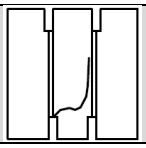 DSS-3-2/K=1.28	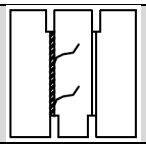 DSS-4-2/K=1.28
B-3	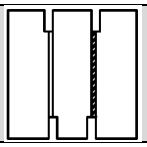 DSS-1-1/K=1.17	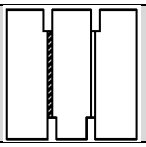 DSS-2-1/K=1.22	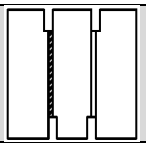 DSS-3-1/K=1.23	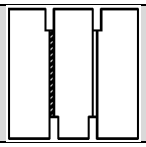 DSS-4-1/K=1.26
	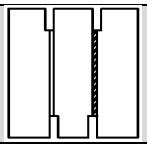 DSS-1-2/K=1.24	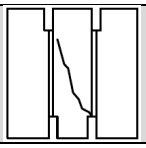 DSS-2-2/K=1.29	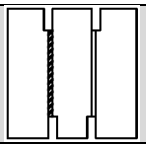 DSS-3-2/K-1.16	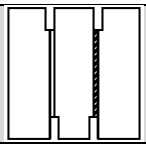 DSS-4-2/K=1.34
B-4	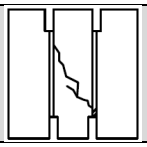 DSS-1-1/K=0.90	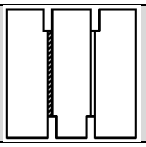 DSS-2-1/K=0.94	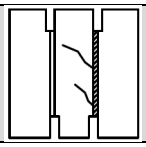 DSS-3-1/K=1.09	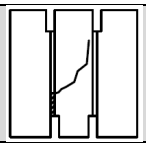 DSS-4-1/K= -
	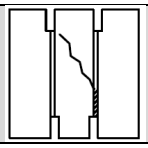 DSS-1-2/K= -	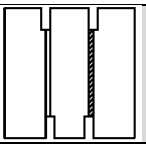 DSS-2-2/K=0.97	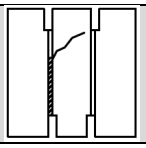 DSS-3-2/K=0.06	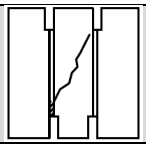 DSS-4-2/K=1.17

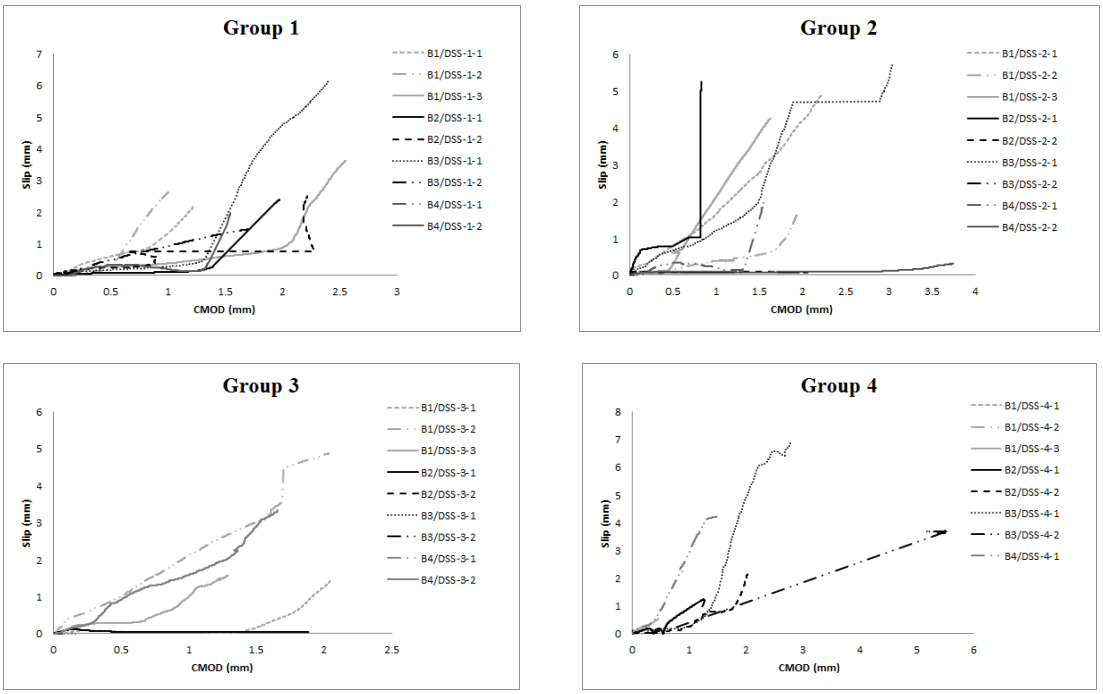

Fig. 14 Slip vs. crack mouth opening displacement relationship

For most of the specimens in group 2 and 3, the slip has started at the higher load. These specimens have shown the lesser slip at the point of pic load which shows the higher toughness. Among some of the specimens, the brittle behavior which might be due to the lower amount of fibers has been observed. Due to the same reason the shear-slip relationship in the case of some specimens is not mentioned. It should be noted that the shear section subjected to the cracks in such specimens (for instance group 4 of specimens in series B-1) were placed only 50 to 100mm far from the end of the beam, so that this behavior is predictable due to the wall effects. Comparing the results, it can be noted that increasing the fracture plane in series B-2 to B-4 of the specimens led to have the better ductility due to collaboration of the higher amount of fibers. Thus all the specimens have been carried the higher shear load for the longer time. However it should be noted that the branching of the cracks could be effective on this behavior.

Table-5 Toughness of the specimens (KN.mm)

Series No.	B-1	B-2	B-3	B-4	B-1	B-2	B-3	B-4	B-1	B-2	B-3	B-4	B-1	B-2	B-3	B-3
Specimen No.	CMOD = 0.1 mm				CMOD = 0.3 mm				CMOD = 0.6 mm				CMOD = 1 mm			
DSS-1-1	2.1	3.4	6.0	1.1	9.3	-	10.3	2.1	14.7	-	12.9	2.8	25.5	-	15.6	3.7
DSS-1-2	0.6	5.3	5.8	-	4.1	13.5	12.9	-	29.1	17.0	25.0	-	60.0	28.2	35.8	-
DSS-1-3	3.0	-	-	-	9.1	-	-	-	10.3	-	-	-	12.0	-	-	-
DSS-2-1	3.6	19.7	5.2	10.0	8	26.1	16.8	18.8	14.0	29.8	27.6	23.4	21.6	87.9	41.4	25.2
DSS-2-2	3.5	9.5	11.6	5.3	6.3	3.4	-	7.1	9.9	15.3	-	7.6	15.7	16.6	-	8.0
DSS-2-3	1.1	-	-	-	1.8	-	-	-	20.5	-	-	-	43.7	-	-	-
DSS-3-1	7.0	-	13.0	-	16.6	-	17.4	-	23.9	7.5	19.7	-	31.9	22.5	22.7	-
DSS-3-2	10.0	1.6	10.2	14.2	16.6	2.6	18.0	24.1	24.0	3.5	38	57.3	31.9	4.8	58.9	78.9
DSS-3-3	5.2	-	-	-	9.3	-	-	-	10.0	-	-	-	20.2	-	-	-
DSS-4-1	0.1	4.8	1.3	-	-	11.8	2.6	-	-	31.5	3.3	-	-	54.3	4.3	-
DSS-4-2	-	1.9	6.9	6.2	5.7	2.8	8.6	20.6	11.6	5.5	10.8	54.5		10.6	-	117
DSS-4-3	-	-	-	-	-	-	-	-	-	-	-	-	-	-	-	-

Fig. 12 shows the crack width vs. slip relationship of all groups of the specimens. In all the specimens, the crack has been started with the negligible horizontal displacement approximately up to 0.2mm slip. Beyond that, the horizontal displacement increased or the crack opened. Progressively the fibers have been activated and the matrix cracked up to the peak load. As soon as the stress transferred through the fibers in the post peak regime, the fracture process localized on the diagonal shear crack band. The slip-crack width relationship has been followed linearly in this stage.
The area under load-slip curves is known as the work of fracture or toughness, "W_{Fs}" [6]. Computing the toughness relative to the slip values in the shear plan allowed the design of the curve shown in Fig. 15. The toughness values show the increasing trend by increasing the slip. It can be noted that the energy required for growth of the crack increases with the crack extension from the notch.

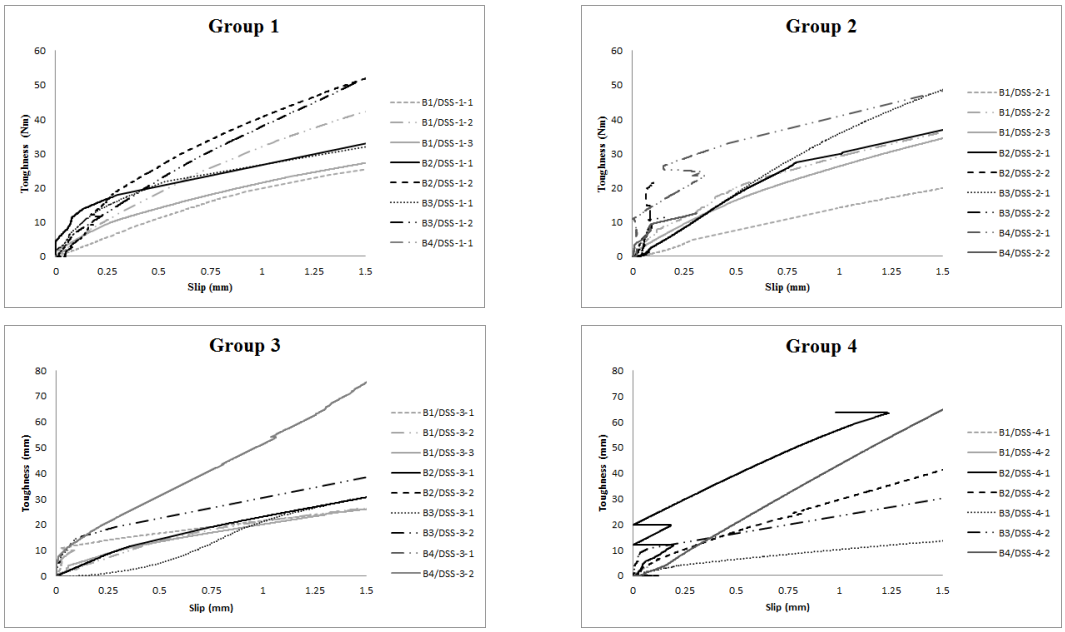

Fig. 15 Toughness-slip relationship

While the slip has been occurred due to the application of the shear load, the CMOD has been observed. Due to the friction between the cracked sections, the test has been followed by the horizontal displacement in addition to the vertical displacement. The fiber bridging not only restrains crack opening but also leads to higher interlocking. Furthermore, the dowel action of the fibers, leads to a lower slip and higher shear transfer. Due to the same reason, the higher load and lower slip has been observed in the case of the specimen including the larger shear surface. The value of specific toughness until a certain slip equivalence with Crack Mouth Opening Displacement (CMOD) of 0.1, 0.3, 0.6 and 1mm, for each specimen can be found in Table-5. Since the dissipated energy has the direct relationship with the toughness of the material; the specimens with the larger shear section (series B-2 to B-4), has shown the higher toughness during the certain slip. Having the toughness value for each of the specimen, the fracture energy per unit area in mode II, "G_{II}" [35] is computed using Eq. 2. The relationship between

the stress intensity factor and strain energy release rate in Mode I and II of fracture, is discussed in annex B.

$$G_{II} = \frac{W_{Fs}}{A_{eff}} \tag{2}$$

where A_{eff} is the effective area of the cross section of the specimen at the failure plane. Consequently the stress intensity factor in mode II of fracture "K_{II}" [5] is achieved for each specimen by the help of Eq. 3.

$$G_{II} = \frac{K_{II}^2(1-\mu^2)}{E} \tag{3}$$

where E is the modulus of elasticity of concrete which is equal to $5000\sqrt{f_c}$ and μ is the Poisson's ratio which is assumed as 0.125 for concrete. The cylinder compressive strength of concrete is used in the calculations as f_c .

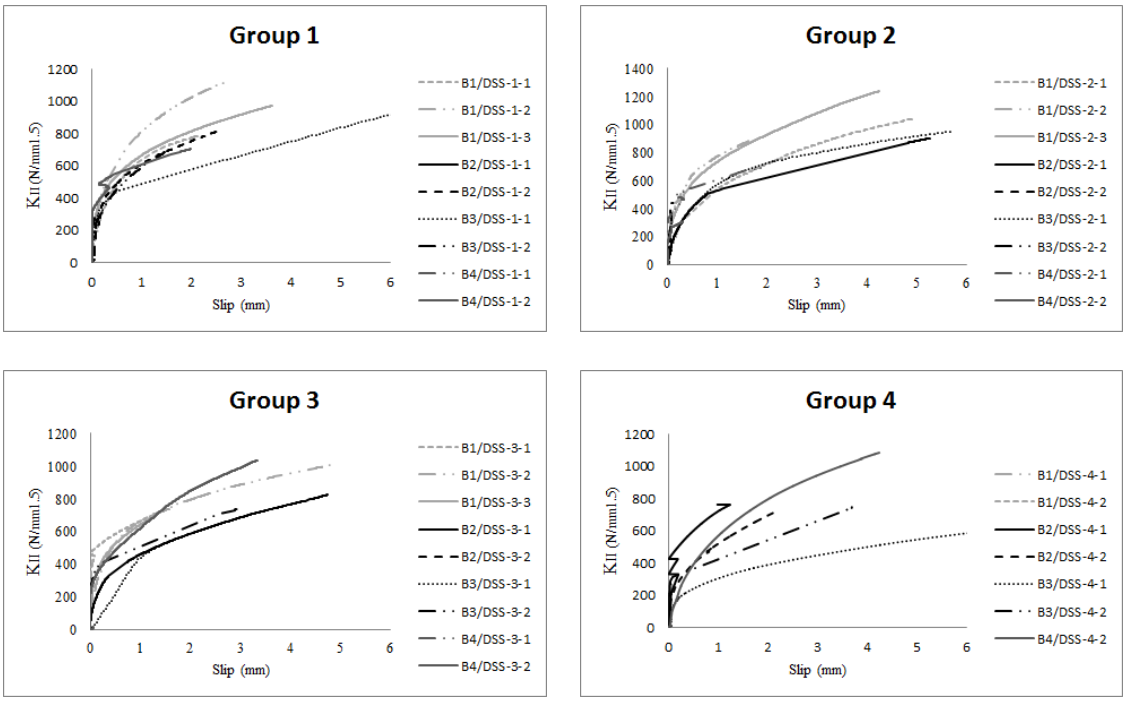

Fig.16 Stress intensity factor vs. slip in mode II of fracture

By the help of Fig. 16 the variation of K_{II} during sliding is comparable for different groups of the specimen. The stress intensity factor of second mode of fracture is shown the higher value in the case of the series B-1, B-4, B-2 and B-3 respectively. Computing the fracture energy and the stress intensity factor of Mode I appears to be sufficient to predict the probability of mixed mode behavior of the specimens. Using Eq. 4 the stress intensity factor "K_I" is calculated in the first mode of fracture and compared with that of Mode II as shown in Table-6.

$$G_I = \frac{K_I^2(1-\mu^2)}{E} \tag{4}$$

where G_I is the fracture energy per unit area in Mode I of fracture. Additionally, G_I can be calculated as the area under stress-CMOD curve for each specimen.

Table-6 Stress intensity factor in Mode I and II of fracture

Series No.	Specimen No.	Mode I		Mode II		G_{Total}
		stress intensity factor "K_I" at P_{pic}	Dissipated energy "G_I" at P_{pic} point	stress intensity factor "K_{II}"At P_{pic}	Dissipated energy "G_{II}" at P_{pic} point	
B-1	DSS-1-1	262.47	1.68	313.89	2.41	4.09
	DSS-1-2	461.21	5.19	412.17	4.15	9.34
	DSS-1-3	314.54	2.42	354.16	3.06	5.48
	DSS-2-1	174.99	0.75	287.15	2.01	2.76
	DSS-2-2	344.96	2.91	325.34	2.58	5.49
	DSS-2-3	357.2	3.12	155.55	0.59	3.71
	DSS-3-1	216.54	1.15	439.95	4.73	5.88
	DSS-3-2	176.72	0.76	428.26	4.47	5.23
	DSS-3-3	194.52	0.92	401.87	3.94	4.86
	DSS-4-1	123.13	0.37	232.93	1.32	1.69
	DSS-4-2	140.94	0.49	-	-	-
	DSS-4-3	-	-	-	-	-
B-2	DSS-1-1	216.73	1.15	275.79	1.85	3.00
	DSS-1-2	354.89	3.08	368.88	3.32	6.31
	DSS-2-1	145.50	0.52	319.73	2.46	2.98
	DSS-2-2	276.28	1.86	332.29	2.69	4.55
	DSS-3-1	254.31	1.58	-	-	1.58
	DSS-3-2	202.36	0.99	147.26	0.53	1.52
	DSS-4-1	-	-	-	-	-
	DSS-4-2	313.98	2.41	325.43	2.59	5.00
B-3	DSS-1-1	247.07	1.49	283.83	1.96	3.45
	DSS-1-2	205.16	1.03	240.03	1.41	2.44
	DSS-2-1	269.28	1.77	321.65	2.53	4.30
	DSS-2-2	177.24	0.77	276.31	1.86	2.63
	DSS-3-1	257.45	1.62	380.79	3.54	5.16
	DSS-3-2	172.04	0.72	236.14	1.36	2.08
	DSS-4-1	286.55	2.01	148.00	0.53	2.54
	DSS-4-2	238.89	1.39	261.88	1.67	3.06
B-4	DSS-1-1	311.69	2.37	130.79	0.41	2.78
	DSS-1-2	-	-	-	-	-
	DSS-2-1	193.00	0.91	301.00	2.21	3.12
	DSS-2-2	191.73	0.90	198.38	0.96	1.86
	DSS-3-1	19.05	0.01	15.92	0.01	0.02
	DSS-3-2	248.34	1.51	354.78	3.10	4.61
	DSS-4-1	-	-	-	-	-
	DSS-4-2	260.79	1.66	253.99	1.58	3.24

Since K_{II}/K_I ratios are relatively small in the case of all series of specimens (see annex C), it can be concluded that the cracks tend to fracture in both modes I and II configurations under combined normal and shear stress states.
The total dissipated energy can be calculated as the summation of the energy released in Mode I and II of fracture as illustrated in Table-6.

It should be mentioned that since the cracks favor to follow the direction with lower stress localization, there should be a suitable equilibrium between the thickness of the specimen and the width of shear plane to design the specimen configuration. To direct the crack along the vertical ligament, the thickness of the specimen " b "should be at least 2.5 times of the shear plan width "a" . This ratio has been taken in to consideration in the case of series B-1 of the specimens. However having the pure shear for the concrete specimen includes the high amount of steel fibers is not the easy task.
According to the results achieved in the present study, it is assume that for observing Mode II of fracture, series B-1 of the specimen can be improved.
Fig.17 shows the stress propagation due to loading the understudy specimen. During loading the specimen, the compressive stress propagates along the ligaments, while the tensile stresses try to open the ligament horizontally. Choosing the proper dimension for the shear plan can be helpful for observing the slip, before a big CMOD takes place. Thus the thickness of the specimen and the distance between the notches of the specimen should be carefully designed.

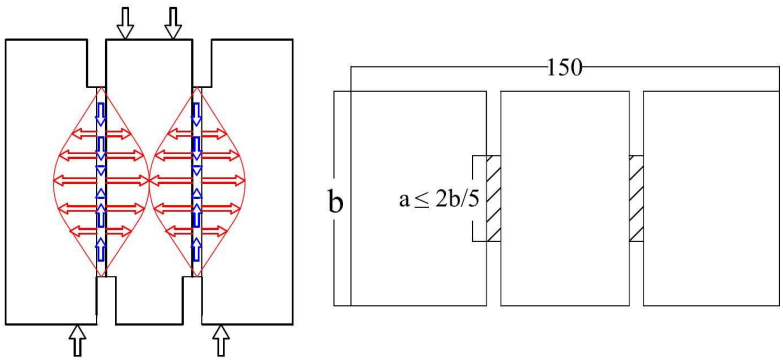

Fig.17 Stress propagation (left) top view of the specimen (right)

5.2 Fiber Structure in the Composite Matrix

After detecting the fracture behavior of DSSs, the image analyzing has performed for the section parallel to the ligament along which the crack took place. The same section has been taken in to consideration in the case of the specimens with the crack branching. Table-7 includes the fiber density " $N_f^{\parallel}$," which is obtained from the analyzed cross sections parallel to the crack surface of the DSS (see Fig.7(b)) using the captured images. In Table-7, $\breve{N}_f^{\parallel}$ is defined as the minimum fiber density. Moreover, the theoretical fiber density for each series assuming a three-dimensional isotropic uniform random fiber distribution " N_f^{3D} ", is also comprised. This analytical expression is computed as Eq. (5) [36].

$$N_f^{3D} = \eta . \frac{V_f}{A_f} \tag{5}$$

where η , $A_f\,[mm^2]$ and $V_f\,[Vol._{-}\%]$ are respectively a dimensionless orientation factor, the cross sectional area of a single fiber and the volumetric fraction of fibers.

Table-7 Density of the fibers located on the analyzed sections

Series No.	Specimen No.	N_f^{3D} $\frac{Fiber}{cm^2}$	$N_f^{\parallel}$ $\frac{Fiber}{cm^2}$	CoV (%)	$\breve{N}_f^{\parallel}$ $Fiber/cm^2$
	DSS-1-1		4.550		
	DSS-1-2		5.050		
	DSS-1-3		5.900		
	DSS-2-1		4.850		
	DSS-2-2		3.700		
	DSS-2-3		4.800		
B-1	DSS-3-1	2.726	4.300	11.552	3.700
	DSS-3-2		4.450		
	DSS-3-3		5.100		
	DSS-4-1		4.750		
	DSS-4-2		4.250		
	DSS-4-3		4.550		
	Average		**4.688**		
	DSS-1-1		3.222		
	DSS-1-2		4.067		
	DSS-2-1		5.222		
	DSS-2-2		4.222		
B-2	DSS-3-1	2.726	3.800	21.304	2.467
	DSS-3-2		4.133		
	DSS-4-1		2.467		
	DSS-4-2		3.422		
	Average		**3.819**		
	DSS-1-1		3.289		
	DSS-1-2		4.067		
	DSS-2-1		5.089		
	DSS-2-2		4.378		
B-3	DSS-3-1	2.726	4.533	19.766	2.689
	DSS-3-2		3.556		
	DSS-4-1		3.556		
	DSS-4-2		2.689		
	Average		**3.894**		
	DSS-1-1		3.360		
	DSS-1-2		2.580		
	DSS-2-1		5.120		
	DSS-2-2		4.280		
B-4	DSS-3-1	2.726	4.420	21.296	2.580
	DSS-3-2		3.760		
	DSS-4-1		3.560		
	DSS-4-2		3.140		
	Average		**3.778**		

The orientation factor is assumed topically the value of 0.5 for a three dimensional isotropic fiber distribution [36]. The fibers can have any orientation in a three-dimensional system, as shown in Fig.18. The reason of accepting 3D orientation for the fibers included in the DSS is that the specimens are prepared using a discretized beam. Thus the fibers had enough space to distribute at 3D orientation.

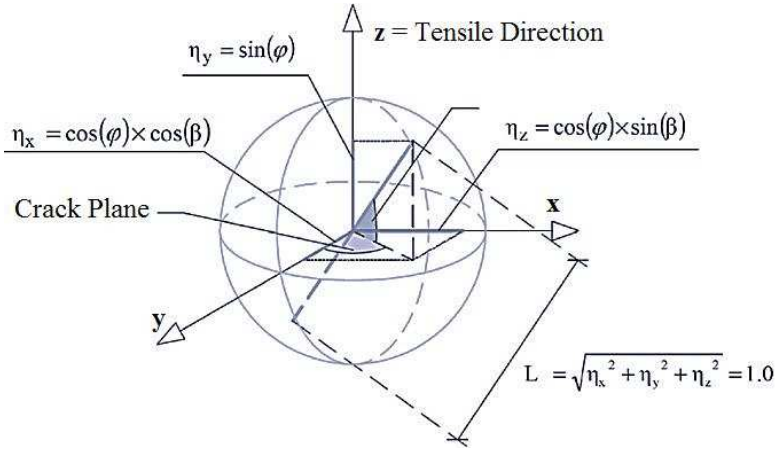

Fig.18 Three-dimensional visualizes of fiber located in the concrete [37]

Since the specimens are made using the same concrete mix, both the average and minimum fiber density are shown the close values in the case of all four series of the specimens. However these values are a bit higher in the case of series B-1. It might be due to collection of the higher amount of the fibers at the location of the understudying sections.

In all series of specimens, the fiber density is higher than that of computed theoretically. Computed "N_f^{3D}" is almost equal to the minimum value of fiber density in each series. The maximum difference between the value of "N_f^{3D}" and "$N_f^{\|}$" is observed in the case of first series of the specimens in which fiber density is 42% higher than that of "N_f^{3D}." The fiber density "$N_f^{\|}$" in other series are almost 29% higher than "N_f^{3D}." The variation of the results "CoV," in all the series of specimens are relatively low, which indicates a good fiber distribution.

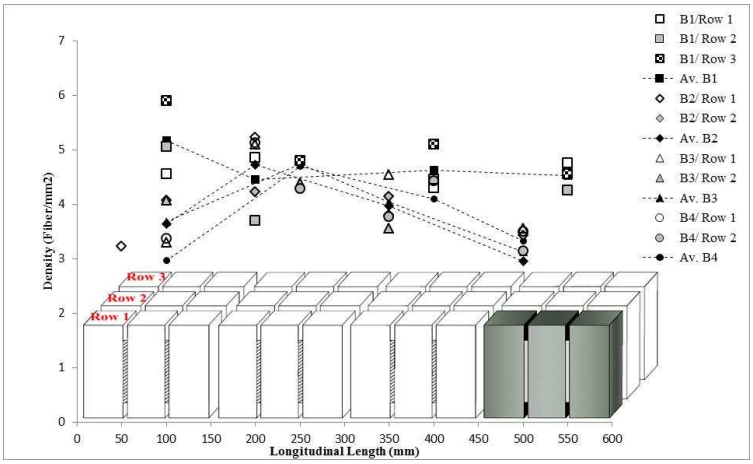

Fig. 19 Fiber density along the beam length

Increase of fiber density can be effectively helpful in the case of intersecting the active crack. This might be due to the high workability of the concrete which make the fibers to alignment along the beams or locating perpendicular to the shear plan of DSSs. The

walls of the prismatic molds are also effective on the orientation of the fibers along the beam.
The fiber density located perpendicular to the shear plane of all the DSSs along the beam is depicted as Fig.19. In general, there is no significant variation of the fiber density along the beams which is due to the good flowability of the fibers. The marginally increase of fiber density located at the middle groups (group 2 and 3) in all series of specimens is observed.
Considering that the particles in images are projectiles of the circular cross-section of fibers, the orientation angles can be obtained. On the cross section of the FRC element the fiber section can be found as a full circle when the longitudinal axis is perpendicular to the cross section. In the other situations the fiber cross section looks like an ellipse.
The fiber orientation can be characterized using the in-plane angle " θ " and the out-plane angle " φ " which are shone in Fig.20. Based upon the image analyzing procedure of the elliptical axis of the intersected fibers, the orientation factor can be determined with the ascertained out-plane angle using Eq. (6) [36].

$$\eta_{img} = \frac{1}{N_f} . \sum_{i=1}^{N_f} cos\theta_i \qquad (6)$$

where $N_f \left[\frac{1}{mm^2}\right]$ is the number of fibers present in a certain cross section and θ is the out-plane angle, i.e. angle between the fiber longitudinal axis and the loading direction.
The dimensionless orientation factor "η" which has already accepted as 0.5 for determining N_f^{3D}; can also be determined as Eq. (7) [36].

$$\eta_{exp} = N_f . \frac{A_f}{V_f} \qquad (7)$$

Table-8 shows the value of orientation factor for all the specimens. The average orientation factor " η_{exp} " is shown almost the same value for series B-2 to B-4 of the specimens while the higher value is observed in the case of series B-1. This can be ascribed to the collection of higher number of fibers at the analyzed section which leads to compute the higher orientation factor for these series of the specimens.
In the bending tests, when the orientation angle which is related to the tensile stress direction (see Fig.20) is around 0 to 30^0; the fiber efficiency has the higher value [36]. The same angles can be suitable for having the best fiber efficiency in the case of understudy tests. Because the angle between the fiber longitudinal axis and the loading direction in these tests is the same as that of bending tests (see Fig. 17).

Table-8 Fiber orientation factors on the prismatic specimens

Series No.	Specimen No.	θ (^{0})	η_{exp}	CoV (%)	η_{img}	CoV (%)
	DSS-1-1	39.14	0.836		0.754	
	DSS-1-2	45.42	0.927		0.678	
	DSS-1-3	45.29	1.083		0.673	
	DSS-2-1	46.11	0.891		0.675	
	DSS-2-2	44.89	0.679		0.684	
	DSS-2-3	39.58	0.881		0.754	
B-1	DSS-3-1	39.90	0.790	11.552	0.745	4.891
	DSS-3-2	46.41	0.817		0.663	
	DSS-3-3	41.62	0.937		0.717	
	DSS-4-1	40.37	0.872		0.742	
	DSS-4-2	44.30	0.780		0.693	
	DSS-4-3	44.68	0.836		0.691	
	Average	**43.14**	**0.861**		**0.706**	
	DSS-1-1	38.26	0.591		0.758	
	DSS-1-2	38.54	0.746		0.760	
	DSS-2-1	34.49	0.958		0.805	
	DSS-2-2	38.89	0.775		0.738	
B-2	DSS-3-1	34.28	0.697	21.304	0.801	4.843
	DSS-3-2	36.79	0.758		0.769	
	DSS-4-1	44.30	0.452		0.690	
	DSS-4-2	39.75	0.628		0.743	
	Average	**38.16**	**0.701**		**0.758**	
	DSS-1-1	38.12	0.603		0.763	
	DSS-1-2	38.54	0.746		0.760	
	DSS-2-1	37.13	0.934		0.767	
	DSS-2-2	35.14	0.803		0.791	
B-3	DSS-3-1	36.77	0.832	19.766	0.774	4.034
	DSS-3-2	30.81	0.652		0.828	
	DSS-4-1	37.63	0.652		0.770	
	DSS-4-2	41.67	0.493		0.717	
	Average	**36.98**	**0.714**		**0.771**	
	DSS-1-1	40.38	0.616		0.744	
	DSS-1-2	40.05	0.473		0.739	
	DSS-2-1	37.51	0.939		0.767	
	DSS-2-2	31.52	0.785		0.822	
B-4	DSS-3-1	38.29	0.811	21.296	0.761	3.403
	DSS-3-2	38.37	0.690		0.757	
	DSS-4-1	39.01	0.653		0.752	
	DSS-4-2	39.27	0.576		0.752	
	Average	**38.05**	**0.693**		**0.762**	

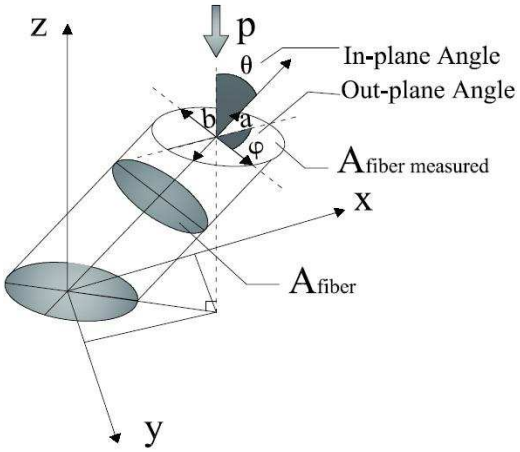

Fig. 20 Orientation angle of a fiber

The area of ellipse in cross section (visible area of fiber) and the real area of fiber in circle were used to determine the angle of inclination [36 and 37]

Among 4 series of the specimens it is found that the fibers are oriented at the angle of almost 38° in series B-2 to B-4. It makes the fibers to have the higher value of η_{img} in the said series as compare to that of series B-1 oriented at the angle of 48^0. The relationship between the fiber density and the orientation factor computed from the cross section image analysis "η_{img}" is represented In Fig.21.

Previous researches [36] pointed out that, there is the marginal increase in the orientation factor by increasing the density of the fibers. However, the results show that, although the fiber density of the first series of the specimens is higher as compare to that of the other series, the orientation factor of this series is lower a bit. The most effective parameter on the orientation factor is the angle corresponds to the fiber alignment with regard to the loading direction.

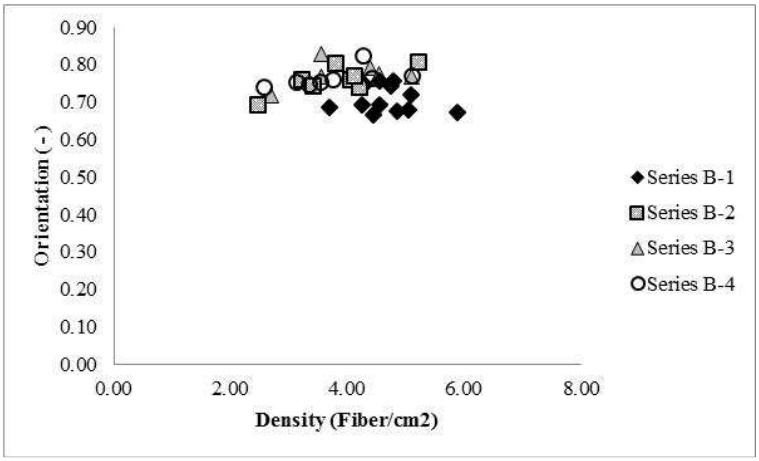

Fig. 21 Relationship between the fiber density and orientation factor

Unlike the preliminary assumption, the fiber density in the first series of specimens has the highest value as compare to the other series (see Table-7). So that, the brittle

behavior of DSS-4-2 in series B-1 and the higher rate of fracture of all the specimens included in the same series cannot be due to lack of fibers intersecting the crack.
The other factor can be controlled to detect the reason of such a behavior is the orientation of the fibers. Among all the specimens of series B-1 the specimens included in group 4, have the lowest orientation factor. It means that the fibers are not oriented at the suitable angle to resist the crack and decrease the rate of failure effectively. On the other hand all the specimens of series B-1 are included a very small shear plane. Thus the number of the fibers should be collaborated to observe the ductile behavior of the specimens is not sufficient.
Similarly the ductile behavior of the other series of the specimen and the slower rate of fracture in these series can be justified. The larger shear section case the better ductility in the case of series B-4 as compare to that of series B-2 and B-3. The fiber density and the orientation factor is almost the same for the specimens of all these series. It can be also visible in the relationship between pic load and fiber density as well as that of the slip and fiber density as shown in Fig.22 (a) and (b) respectively. Although the fiber density is higher in the case of the first series of the specimens, the higher pic load and lower slip is observed in the case of most of the specimens in series B-2 to B-4 which include the larger shear section. However, there are some specimens such as DSS-1-2, 3-1 and 4-1 of series B-4, included the least orientation factor which is caused the lower pick load and higher slip as compare to the other specimens of this series. Additionally the low fiber orientation is caused the reduction in the toughness value of the same specimens. The same justifications can be used for the relationship between the stress intensity factor and energy release vs. fiber density in Mode I and II of fracture as shown in annex D.

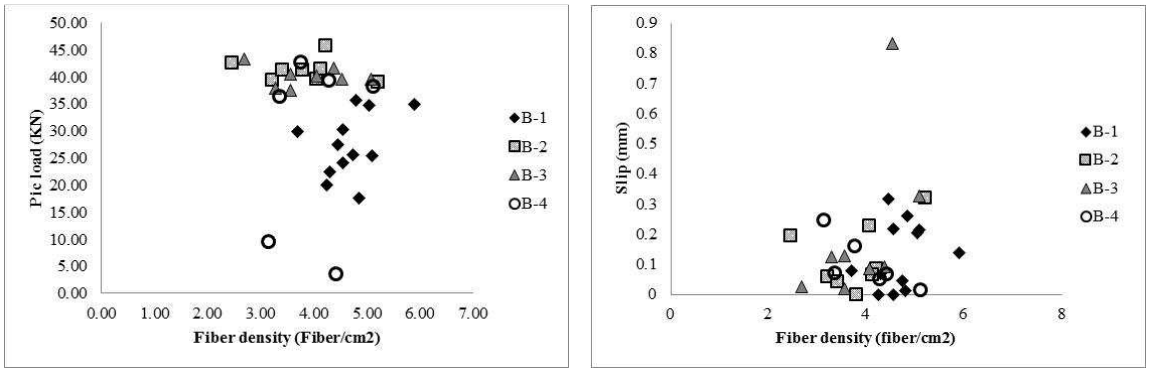

Fig.22 (a) Pic load vs. fiber density (b) Slip vs. fiber density

6 CONCLUSIONS

In the present study, the fracture behavior of FRSCC under direct shear loading is discussed. Based on the tests conducted on the new specimens prepared using the discretized beams, the following results are given:

– The maximum shear stress and consequently the correlation constant “k”, toughness and fracture energy are affected significantly by the amount and the orientation of the fibers. Using the proper SCC can be helpful to find the said factors suitable enough even in the case of the specimens located far from the middle of the beam.

- The micro cracks observed along the ligament of DSS illustrates that Mode II of fracture exists at least on the micro scale. However, computing the relatively small "$\frac{K_{II}}{K_I}$" in the present study, one can be noted that under combined normal and shear stress states, the cracks tend to fracture in both Mode I and II configurations. Thus the designed DSS can be used effectively to characterize the FRSCC under mixed mode of fracture.
- Loading the shear specimens, the linear variation of load vs. slip has been observed up to occurrence of the first crack. It tend to become nonlinear up to the peak load which followed by the sudden drop. The last step might be due to the fact that some steel fiber bridging the crack along the shear plane yielded in tension. This behavior has followed by rupture of the fibers upon increasing the deformation. The descending trend continued gradually up the complete failure.
- The crack width vs. slip relationship of the specimens has been shown the negligible horizontal displacement approximately up to 0.2mm slip. The horizontal displacement started thereafter. Progressively the fibers have been activated and the matrix cracked up to the peak load. As soon as the stress transferred through the fibers in the post peak regime, the fracture process localized on the diagonal shear crack band. The slip-crack width relationship has been followed linearly in this stage. The dowel action of the fibers leads to a lower slip and higher shear transfer. Higher interlocking and restraining the crack opening follows the fiber bridging.
- During loading the specimen, the shear crack propagation is accompanied by compression failure along the ligament after the maximum load. The concrete keeps the fibers more tightly and the bond strength between the fiber and the concrete improves. Thus when fibers are collected at one point rather than the other parts of the specimen, the shear crack may change its direction.
- By varying the thickness of the specimen or the width of the shear plane, the transition between two different failure modes may occur. When the specimen is ticker; crack branching is favored and a crack trajectory develops from the crack tip to the opposite point load. To avoid this phenomenon the ratio of specimen thickness to the width of the shear plan should be taken in to consideration.
- Due to the extended collaboration of the fibers included in the larger shear plane, the smaller slip has been found at the pic load.
- The toughness values show the increasing trend by increasing the slip. The specimens with the larger shear section (series B-2 to B-4) have shown the higher toughness during the certain slip.
- The energy required for growth of the crack increases with the crack extension from the notch.
- Larger fracture plane of the specimens led to have the better ductility due to collaboration of the higher amount of fibers. Thus the specimens of series B-2 to B-4 have carried the higher shear load for the longer time. However it should be noted that the branching of the cracks could be effective on this behavior
- The fiber density measured at the parallel planes "$N_f^{\parallel}$," is considerably higher than the expected theoretical fiber density assuming a 3D isotropic uniform random distribution "N_f^{3D}." The maximum difference between the value of N_f^{3D} and $N_f^{\parallel}$ is observed in the case of first series of the specimens in which the value of fiber

density is 42% higher than that of calculated theoretically. The fiber density shows almost 29% higher value in the case of other series of specimens as compare to that of N_f^{3D}.

- Among 4 series of the specimens, it is found that the fibers are oriented at the angle of almost 38° in series B-2 to B-4. It makes the fibers to have the higher value of η_{img} in the said series as compare to that of series B-1 which oriented at the larger angle .
- Although the fiber density is higher in the case of the first series of the specimens, as compare to the other series, the higher pic load and lower slip is observed in the case of most of the specimens in series B-2 to B-4 which include the larger shear section. It can be noted that in addition to the fiber density, having the collaboration the higher number of fibers is very effective on optimization of the concrete behavior.

ANNEX A

Table-A1 Fracture behavior of the specimens under the shear load

Width of the shear plane = 20mm	 (1) 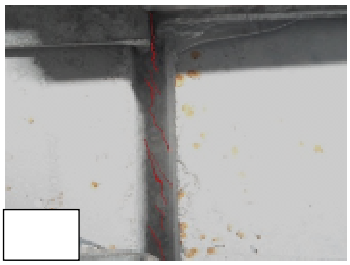  1. Starting the test by applying the shear load which lead to propagation of the tensile stresses along the ligaments; 2. Appearance of the inclined micro cracks along the ligaments, sliding and starting the fiber pull out; and 3. Joining the inclined cracks and providing a shear crack along the ligament. Pull out or rupture of the fibers up to the complete mix mode fracture.	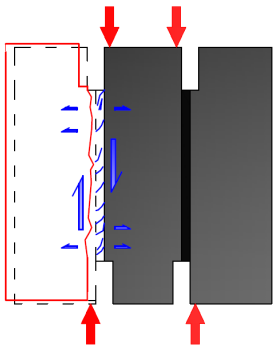
Width of the Shear plane ≥ 45mm	   1. Starting the test by shear loading; the crack favors to follow the maximum circumferential stress criterion; 2. Propagation of the cracks along the ligament and occurrence of the sliding. Branching the crack out of the ligaments which lead to rotation and CMOD; and 3. Increasing the number, length and width of the inclined cracks. Ending up the test by observing the mix mode failure, large sliding and CMOD of the specimen, without any brittle behavior.	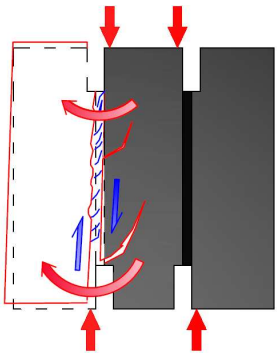

ANNEX B

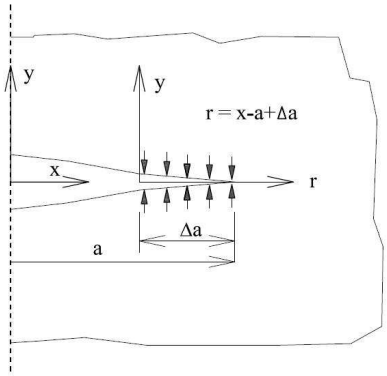

Fig.B1 Closure of crack tip

Fig. B, shows an under tension infinite plate with 2a crack size. Since the crack opening takes place herein the strain energy release rate "G_I" and the stress intensity factor "K_I" of Mode I of fracture can be calculated as Eq.A1:

$$G_I = \frac{2}{\Delta a}\int_0^{\Delta a}\frac{1}{2}\sigma_y v\, dr = \frac{1}{\Delta a}\int \frac{K_I v}{\sqrt{2\pi r}}\, dr \qquad (A1)$$

where v is the displacement in y direction. The factor 2 is due to the fact that the crack has two surfaces and the $\frac{1}{2}$ means that the stress increases from zero in proportion with v.
The value $2v$ is equal to the crack mode displacement. For the infinite plate subjected to tension, the value of v is given as Eq. A2.

$$v = \frac{CMOD}{2} = \frac{2\sigma}{E}\sqrt{a^2 - x^2} = \frac{2K_I}{E}\sqrt{\frac{a^2 - x^2}{\pi a}} \qquad (A2)$$

Since $r = x - a + \Delta a$ the value of v can be defined as:

$$v = \frac{2K_I}{E\sqrt{\pi}}\sqrt{2\,\Delta a - 2r + \frac{2r\,\Delta a}{a} - \frac{r^2}{a}} \cong \frac{2K_I}{E\sqrt{\pi}}\sqrt{2(\Delta a - r)} \qquad (A3)$$

Using the Eq. A1 and A3, the strain energy release rate can be in the form of Eq. A4:

$$G_I = \frac{2K_I^2}{E\,\pi\,\Delta a}\int_0^{\Delta a}\sqrt{\frac{\Delta a - r}{r}}\, dr \qquad (A4)$$

Integrating the above equation and letting Δa approach zero, lead to Eq. A5 for plain strain:

$$G_I = \frac{K_I^2}{E} \qquad (A5)$$

For plain stress, E should be replaced by $(1 - \mu^2)\frac{K_I^2}{E}$, thus the energy release rate ia as follow for the plain strain:

$$G_I = (1 - \mu^2)\frac{K_I^2}{E} \qquad (A6)$$

Similarly, it can be shown that for Mode II of fracture,

$$G_{II} = \begin{cases} \dfrac{K_{II}^2}{E} & \text{For plain stress} \\ (1-\mu^2)\dfrac{K_{II}^2}{E} & \text{For plain strain} \end{cases} \quad (A7)$$

The superposition is used for obtaining the total strain energy in combined crack modes for the plain strain is as Eq. A8.

$$G = G_I + G_{II} = \frac{1-\mu^2}{E}(K_I^2 + K_{II}^2) \quad (A8)$$

ANNEX C

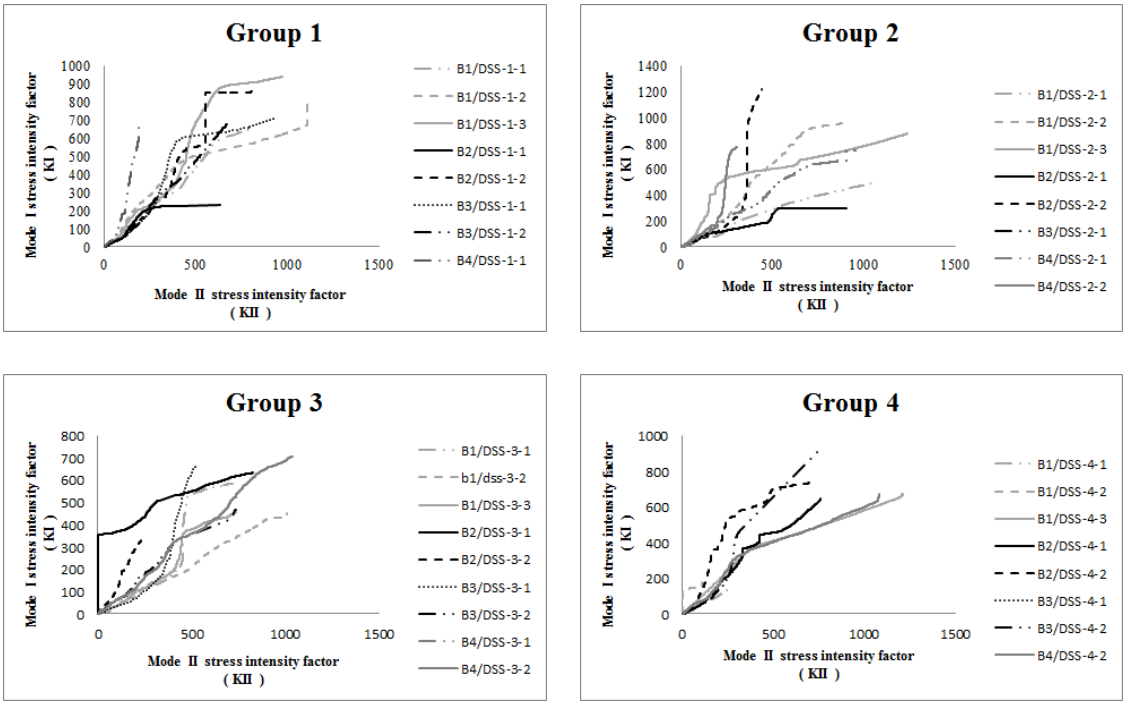

Fig.C1 stress intensity factor of Mode I of fracture vs. that of Mode II

ANNEX D

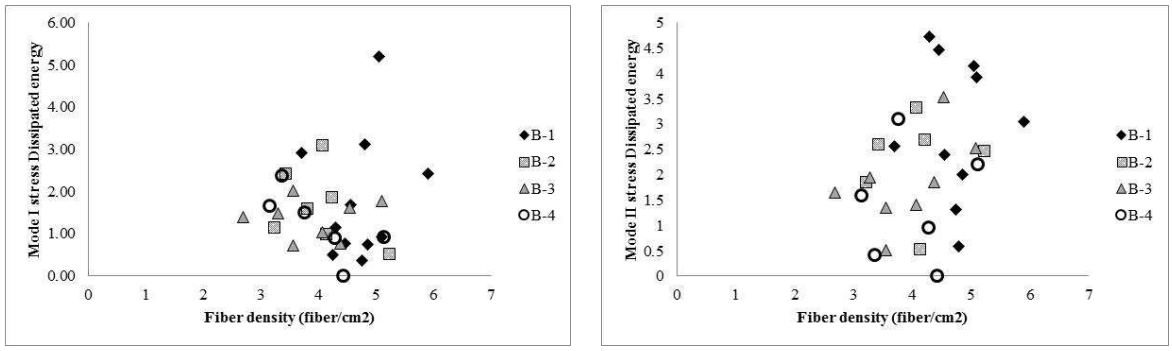

(a) **(b)**

Fig.D1 (a) Stress dissipated energy vs. fiber density in Mode I and (b) Mode II of fracture

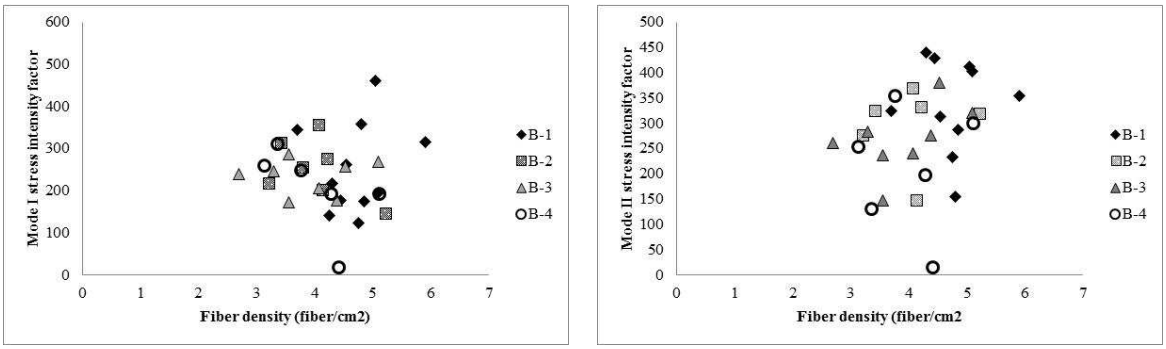

(a) **(b)**

Fig.D2 (a) Stress intensity factor vs. fiber density in Mode I and (b) Mode II of fracture

REFERENCES

[1] Ayatollahi M.R., Asadkarami A., Zakeri M., (2005), "Finite Element Evaluation of Punch-Type Crack Specimens," *International Journal of Pressure Vessels and Piping*, 82, pp 722–728.
[2] Young W.C., (1989), "Roark's Formulas for Stress and Strain," 6th edn., McGraw-Hill, New York,.
[3] Arrea M., Ingraffea A.R., (1982), "Mixed Mode Crack Propagation in Mortar and Concrete," Report No. 81-13, Dept. Structure. Eng., Cornell University, Ithaka, N.Y.
[4] Bazant, Z. P., Pfeiffer, P.A., (1986), "Shear Fracture Tests of Concrete," RILEM Material and Structures, Vol. 19, No. 110, pp 111-121.
[5] Shah S. P., Swartz S. E. and Ouyang C., (1995), "Fracture mechanics of concrete: applications of fracture mechanics to concrete, rock and other quasi-brittle material," A WILEY-INTERSCIENCE PUBLICATION, United State of America.
[6] Rao G. Appa and Rao A. Sreenivasa, (2009), "Toughness indices of steel fiber reinforced concrete under mode II loading," Journal of Material and Structure, 42, pp 1173-1184.
[7] Barros, J. and Antunes, J., (2003), "Experimental characterization of the flexural behavior of steel fiber reinforced concrete according to RILEM TC 162-TDF recommendation," RILEM 162-TDF Workshop, Bochum, Germany, pp 77-90.
[8] Shah, S. P. & Ouyang, C., (1991), "Mechanical Behavior of Fiber-Reinforced Cement-Based Composites," *J. Am. Cerum. Sot.*, 74(11) 2227-2238; pp 2947-2953.
[9] Furlan S. & Hanai J. B., (1997), "Shear Behavior of Fiber Reinforced Concrete Beam," *Cement and Concrete Composites Journal*, 19, pp 359-366.
[10] Oliveira F. L., (2010), "Design-Oriented Constitutive Model for Steel Fiber Reinforced Concrete," Doctoral Thesis, Universitat Politècnica de Catalunya, Departament d´Enginyeria de la Construcció.
[11] Hassanzadeh, M., Hilllerborg, A. and Zhou Fan Ping (1987), "Test of Material Properties in Mixed Mode I and II, in Fracture of Concrete and Rock," RILEM-SEM Int. Conf., Houston (ed. S. P. Shah and S.E. Swartz), pp 353-358.
[12] Keuser, W., (1986), "Kornverzahnung bei Zugbeanspruchung. Forschungskolloquim DAfStb, Darmstadt, pp 13-18, Quoted in "Elfgren F., (1989), "Fracture mechanics of concrete structure from theory to application," RILEM, Technical Committee 90 FMA, RILEM REPORT, Chapman and Hall, USA."
[13] Reinhard H.W., Cornelissen, H.A.W. and Hordijk, D.A., (1987), "Mixed Mode Fracture Test on Concrete, in Fracture of Concrete and Rock," RILEM-SEM Int. Conf., Houston (ed. S.P. Shah and S.E. Swartz), pp 324-337.
[14] Kui, Zhong, (2002), "Mixed model I-II-III fracture criterion and its application to cement mortar," Ph.D. Thesis, Tongji University, M. Eng., National University of Singapore.
[15] Xu, Shilang, Reinhard, Hans W., (2005), "Shear fracture on the basis of fracture mechanics," Otto-Graf-Journal, Vol.16, pp21-78.
[16] Iosipescu, N. (1967), "new accurate procedure for single shear testing of metals," Journal of Material, Vol.2, No.3, pp 537-566.
[17] Ayatollahi M.R., Aliha M.R.M., (2005), "Cracked Brazilian disc specimen subjected to mode II deformation," Engineering Fracture Mechanics, 72, pp 493–503.
[18] Ayatollahi M.R., Aliha M.R.M., (2009), "Analysis of a new specimen for mixed mode fracture tests on brittle materials," Engineering Fracture Mechanics, 76, pp 1563–1573
[19] Mayer C., Eggeler G., Webster G.A. and Peter G., (1994), "Doubel shear creep testing of superalloy sungle crystals at temperatures above 1000 °C," Material Science And Engineering Journal, A199, pp 121-130.
[20] Serrano Erik, (2004), "A Numerical Study of the Shear-Strength-Predicting Capabilities of Steel Specimen for Wood-Adhesive Bonds," International Journal of Adhesion and Adhesives, pp 23-35.
[21] Kumosa M. and Han Y., (1999), "Non-Linear Finite-Element Analysis of Losipescu Specimens," Composites Science and Technology Journal, 59, pp 561-573.
[22] Rao Q., Sun Z. Stephansson O., Li C. and Stillborg B., (2003), "shear fracture (Mode II) of brittle rock," International Journal of Rock Mechanics & Mining Sciences, 40, pp 355-375
[23] Shouler D.R. AND Allwood J.M., (2010), "Design and use of novel sample design for formability testing in pure shear," Journal of Materials Processing Technology, 210, pp 1304-1313.
[24] Hasanpour R., Choupani N., (2009), "Rock fracture characterization using the modified Arcan tests pecimen," International Journal of Rock Mechanics & Mining Sciences, 46, pp 346–354.

[25] Rittel D., Ravichandran G., and Lee S., (2002), "Large Strain Constitutive Behavior of OFHC Copper over a Wide Range of Strain Rates Using the Shear Compression Specimen," Mechanics of Materials journal, 34, pp 627–642.
[26] Peirs J., Verleysen P., Degrieck J., Coghe F., (2010), "The use of hat-shaped specimens to study the high strain rate shear behaviour of Ti–6Al–4V," International Journal of Impact Engineering, 37,703–714.
[27] Arcan M., Hashin Z., Voloshin A., (1977), "A Method to Produce Uniform Plane-Stress States with Application to Fiber-Reinforced Materials," Experimental Mechanics journal, pp 141-146.
[28] Hisabe N., Yoshitake I., Tanaka H., and Hamada S., (2006), "Mechanical behavior of fiber reinforced concrete element subjected to pure shearing stress," International RILEM workshop on High performance fiber reinforced cementitious composites in structural applications, RILEM Publication SARL, pp 375-381.
[29] Sagaseta J. and Vollum R. L., (2011), "Influence of aggregate fracture on shear transfer through cracks in reinforced concrete," Magazine of Concrete Reinforced, Vol. 63, Issue 2, pp 119-137.
[30] Zdenek P. Bazan, Prat Pere C. and Tabbara Mazen R., (1990), "Antiplane Shear Facture Tests (Mode II)," ACI Material Journal, No. 87-M7, pp 12-19.
[31] Xu S., Reinhardt H. W. and Gappoev M., (1996), "Mode II fracture testing method for highly orthotropic materials like wood," International Journal of Fracture, 75, pp 185-214.
[32] RILEM TC 162-TDF: Test and design method for steel fiber reinforced concrete. (2002), Material and Structures, Vol. 35, pp 579-582.
[33] Banzant Z. P. and Pfeiffer P. A., (1986), "Shear fracture tests of concrete," *Materiaux et Constructions*, Vol. 19, No. 110, pp 111-121.
[34] Foster J. Stephen, (2009), "The application of steel-fibres as concrete reinforcement in Australia: from material to structure," *Journal of Materials and Structures, RILEM*, 42:1209–1220.
[35] Vall Mariano and Buyukozturk Oral, (1993), "Behavior of fiber reinforced high-strength concrete under direct shear," ACI Material Journal, Title No. 90-M13, pp 122-133.
[36] Cunha V., (2010), "Steel Fibre Reinforced Self-Compacting Concrete (from Micro-Mechanics to Composite Behaviour)," Doctoral thesis, University of Minho, ISBN: 978-972-8692-44-5.
[37] Laranjeira F., Aguado A, Molins C., Grünewald S., Walraven J., Cavalaro S., (2012), "Framework to predict the orientation of fibers in FRC: A novel philosophy," *Journal of Cement and Concrete Research*, *ELSEVIER*, 42, pp 752–768.